

# Broadband 3D-Printed Polarizer based on Metallic Transverse Electro-Magnetic Unit-Cells

C. Molero, *Member, IEEE*, H. Legay, T. Pierré, and M. García-Vigueras, *Member, IEEE*,

**Abstract**—This manuscript presents a three-dimensional polarizing screen that converts linear to circular polarization in a broadband frequency range. The conceived unit-cells are fully metallic and based on structures that support transverse electromagnetic modes. Such cells have been specially conceived to be manufactured through metal three-dimensional printing based on Selective Laser Melting. This is the first time that a polarizing structure presents such a broadband behavior without the use of dielectric materials. In addition, this is the first successful proof of concept of additive manufacturing in the context of metallic periodic surfaces, which is enabled by the use of a co-design approach. The present proposal is validated through the design and manufacturing of a prototype operating in K- and Ka-bands. Successful experimental results are reported.

**Index Terms**—3-D periodic structures, polarizers, additive manufacturing, Selective Laser Melting, equivalent circuits.

## I. INTRODUCTION

MODERN 3D printing techniques have stimulated researchers to push the envelope on innovation in antenna design. Particularly, the analysis of 3D periodic structures has been boosted in the past decades due to the multiple degrees of freedom that they provide in comparison to their 2D counterparts. In addition to enhanced design freedom, 3D-printing allows to envision monolithic prototyping, thus avoiding the cost, time and potential performance degradation of multi-piece manufacturing, mechanical assembly and joints.

So far, 3D periodic structures have found a wide range of applications. The most common one is related to the implementation of spatial filters. For example, in [1]–[3] exotic architectures provide passband response thanks to the excitation of their own resonances. Ultrawideband transmission response is reported in [4] with the help of bifilar lines, and in [5] basing on sub-wavelength units. Structures combining passband and rejection bands are reported in [6], employing slotlines. Band-gap or band-stop operation has been reported with diverse motivation, pursuing stable angular response [7], [8], dual-polarization operation [9] or multi-band performance [10]. Applications involving absorbers have been covered by 3D structures as well [11]–[13]. The design reported in [14] profits from 3D-printing technologies and the model in [15] employs ferrites to enhance the absorption process. 3D-printed lenses are presented in [16]. Frequency selective surfaces operating at low teraherzs built with aerosol jet 3D printing [17],

and metallodielectric structures with tunable operation [18] have been recently proposed. Finally, polarization conversion has also been implemented employing 3D architectures. Such is the case of the rotator reported in [19], or the circular polarizers of multiple types [20]–[22].

Special attention deserves the work published by some of the authors of the present paper in [23], [24], which report for the first time a concept to conceive full-metal polarizing screens. The employed unit-cells are based on sections of rectangular waveguides operating below cutoff that are perforated with resonant slots in their walls. The operation of the cells can be explained based on evanescent filter theory, where the pass-band response is synthesized by means of controlling the number, size and mutual coupling of the cascaded resonators. Versatile performance can be achieved, and for example, the model proposed in [24], allows to obtain dual-band operation with orthogonal sense of polarization in each of the bands. The main drawback of such proposal is its narrow band operation, which is inherent to the dispersion of the employed resonant cells.

Broadband polarizing screens in the literature are conceived basing on a rather different operation principle, and they are typically implemented with stacks of 2D periodic surfaces. Such principle was employed for the first time by L. Young et al [25], when they introduced the meander-line gratings. Instead of employing resonant elements, polarization conversion is attained in this case by properly controlling the quasi-static behavior of the periodic array. In particular, orthogonal electric field components suffer either quasi-static capacitive or inductive behaviors when they pass through the meander-lines, which allow to synthesize the desired 90-degrees phase delay between them in a broad bandwidth. The geometry of the meanders has been extensively studied and applied in several scenarios [26]–[30]. Other geometries have been proposed that implement the same principle, such is the case of [31]–[33] with classical strips, [34] exploiting the concept of miniaturization, or [35]. The main drawbacks of these structures is related to their inherent 2D character, which limits the simultaneous and independent manipulation of the orthogonal modes. Furthermore, the typical manufacturing process is based on PCB standard techniques which employ dielectric materials.

To the best knowledge of these authors, broadband full-metal polarizing screens have not yet been proposed in the literature. There are two main issues to solve when aiming at getting rid of dielectric materials. Firstly: The need for a monolithic architecture, since supports are not allowed and there is no possibility to have non-connected "flying" parts.

Manuscript received XX - XX - XXXX; revised XX - XX - XXXX; accepted XX - XX - XXXX. This work was supported in part by the Region de Bretagne, Thales Alenia Space, Thales group through their KTD-Hardware and the European Union through the European Regional Development Fund, and by Ministry of Higher Education and Research, Brittany Rennes Metropole, through the CPER Project SOPHIE / STIC Ondes.

This is an important constraint for RF designers. Secondly: Operation with electrically small periodicity, in order to avoid grating lobes and be robust with respect to the angle of incidence. This is easily done employing dielectric materials, thanks to the miniaturization brought by the permittivity. In the case of full-metal solution, there is a trade-off to overcome, because a cell with small periodicity that is self-supported tends to be very reflective to the impinging waves.

The enabling strategy here proposed is to address both these issues counting on the "third dimension" thus profiting from greater design freedom. 3D-printing is the technology that allows for the greatest freedom, but it also brings some limitations, specially those related to the appearance of undesired mechanical supports. To succeed in such prototyping, the constraints have to be considered early in the design process, and the use of a co-design methodology is imposed.

An original solution is here proposed consisting in the use of monolithic 3D unit-cells that are low dispersive thanks to the support of transverse electro-magnetic (TEM) modes [36]. The scenario is clearly different from that in [24], which was based on the excitation of evanescent TE modes in rectangular waveguides. An equivalent circuit is built to explain the behavior of the proposed TEM-cell and to synthesize the desired polarizing functionality. The circuit methodology is explained in detail and it allows to extend the application of the cell to other functionalities such as frequency filtering, impedance matching or versatile polarization control.

The proposed concept is validated experimentally through the prototyping and measurement of an array of cells built in Titanium through Selective Laser Melting (SLM) 3D-printing. So far, SLM is the the only technique allowing for high precision employing metallic powder, but the limitations related to the orientation of the piece are greater than printing with plastics [37], [38]. This manuscript represents the first proof of concept of a periodic structure built with SLM. The success of the prototyping relies in the fact that the unit-cell is conceived from the beginning to be 3D-printed and the employed co-design methodology is driven by a simple circuit model. The measured performance shows a minimum of 37.8% operation bandwidth for normal incidence which reduces to 22.2% for 30° TE incidence. It should be highlighted that such bandwidth percentages have not yet been reported in the open literature considering metallic structures. Moreover, the dielectric polarizers reaching such bandwidths need multiple layers of PCB.

The present proposal is suitable for space application and could be also used in other harsh environments, such as in defense outdoor platforms. Since it does not need any supporting material, dielectric losses are avoided as well as other associated undesirable phenomena related to the stringent space environment (all issues related to radiation, outgassing, aging, large range of temperatures resulting in multi-material thermal expansion, variation of the dielectric constant with temperature...). Additionally, this work is well suited to applications that avoid assembly steps and that privilege the use of devices that can be built in a single piece.

This paper is organized as follows. Section II describes the TEM-cell in a progressive way together with the associated

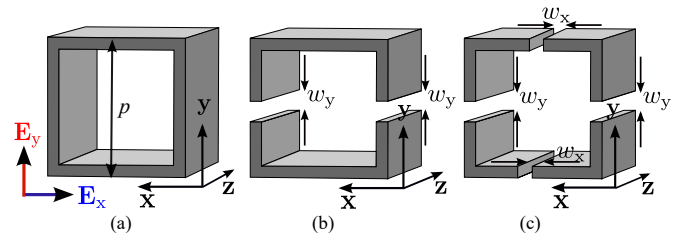


Fig. 1. (a) Initial squared unit cell. (b) Cell evolution that supports y-polarized TEM modes. (c) Final unit-cell supporting TEM modes for both x and y polarizations.

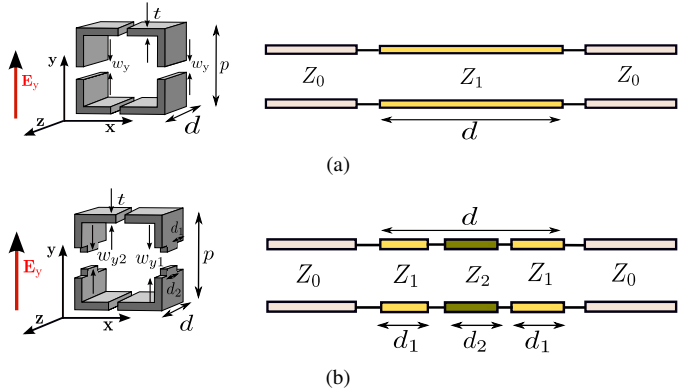


Fig. 2. Circuit modeling of vertical excitation in unit cells that are (a) uniform along  $z$ , (b) employ stepped slits along  $z$ .

equivalent circuits. The circuit model will be extended to cover the inclusion of metallic columns (loads). Section III describes the design procedure of a polarizer covering both the K and Ka bands. Section IV explains the modifications that are performed to the structure in order to enable manufacturing through SLM. Finally, Section V shows the fabricated prototype, and the measured results obtained in the laboratory.

## II. UNIT-CELL BASED ON TEM WAVEGUIDE

### A. Basic structure of TEM-cell

The basic shape of the proposed unit-cell is shown in Fig. 1(c), it consists of a metallic rectangular waveguide that has a longitudinal slit on each wall (of widths  $w_x$  and  $w_y$  when they are parallel to the  $x$  and  $y$  axis, respectively). The unit cell is dual-polarized, and it can be illuminated by both x and y-polarized plane waves (corresponding respectively to the so called H-pol and V-pol). The way the cell is progressively built is illustrated in Fig. 1, using as starting point the classical square waveguide and illumination in the normal direction. The cell section (parameter  $p$ ) is smaller than  $\lambda/2$  at the operation frequency, in order to operate well below the appearance of grating lobes. The slits in the lateral walls are inserted in order to modify the nature of the fundamental modal solutions of the squared structure, which are of TE nature. By including first the slits of width  $w_y$  (see Fig. 1(b)), the cell supports y-polarized TEM modes, which propagate and are excited by vertically polarized impinging waves (V-pol). The orthogonal component (H-pol) still encounters a virtual square waveguide when arriving to the cell, thus exciting a  $TE_{01}$  mode that operates below cutoff.

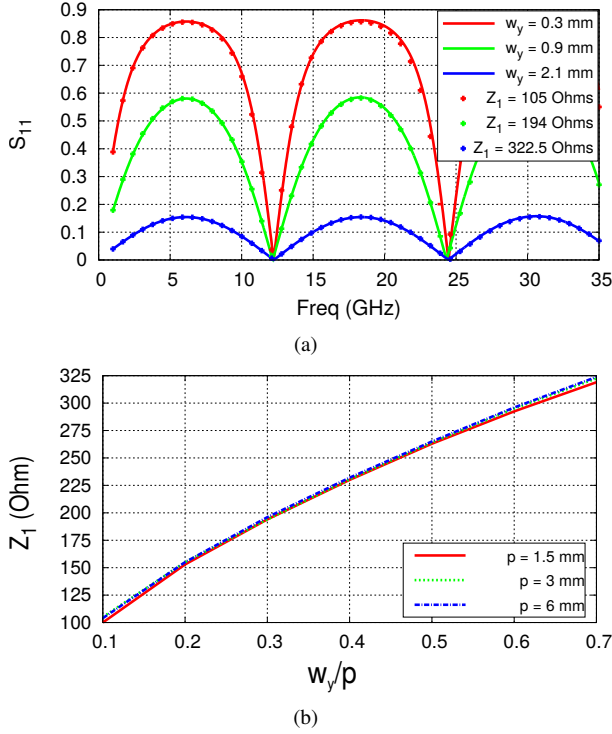


Fig. 3. Analysis of the scenario in Fig. 2(a) with parameters  $p = 3$  mm,  $t = 0.25$  mm and  $d = 12$  mm. (a) Reflection coefficient versus frequency. Results from CST/circuit are represented by continuous/dotted lines. (b) Characteristic-impedance value of the equivalent transmission line as a function of the slit width  $w_y$ , normalized to the period.

To extend the excitation of TEM modes to horizontal polarization, the same operation is carried out in the top/bottom walls, obtaining the cell depicted in Fig. 1(c). The slit size is now defined by the parameter  $w_x$ . The cell presents two main degrees of freedom:  $w_y$  and  $w_x$ , that control respectively and independently, the interaction with V-pol and H-pol waves.

### B. Impedance control of TEM-cell

The impedance control of the TEM-cell can be addressed by basing on classical transmission-line theory, and it is illustrated in Fig. 2 for the case of V-pol. The case of H-pol is not explained here for the sake of conciseness; it can be addressed analogously by basing on the same topology of equivalent circuit. The case of Fig. 2(a) considers a unit cell whose geometry is uniform along the  $z$ -direction, and it can be modelled by a simple circuit consisting on a portion of transmission line of length  $d$  and impedance  $Z_1$ . In Fig. 2(b) stepped slits are introduced in the lateral walls of the cell, thus being circuitually interpreted as a concatenation of transmission-line sections of impedance  $Z_1$  and  $Z_2$ . In the following, the behavior of such cells is explained and the proposed equivalent models are validated. In all cases, the characteristic impedance of the line is numerically estimated with the help of the full-wave solver CST.

The results in Fig. 3 concern the uniform scenario described in Fig. 2(a); its  $S_{11}$  is plotted for different values of  $w_y$  in Fig. 3(a). Two points of null reflection can be identified in all curves for the same frequency points, which appear

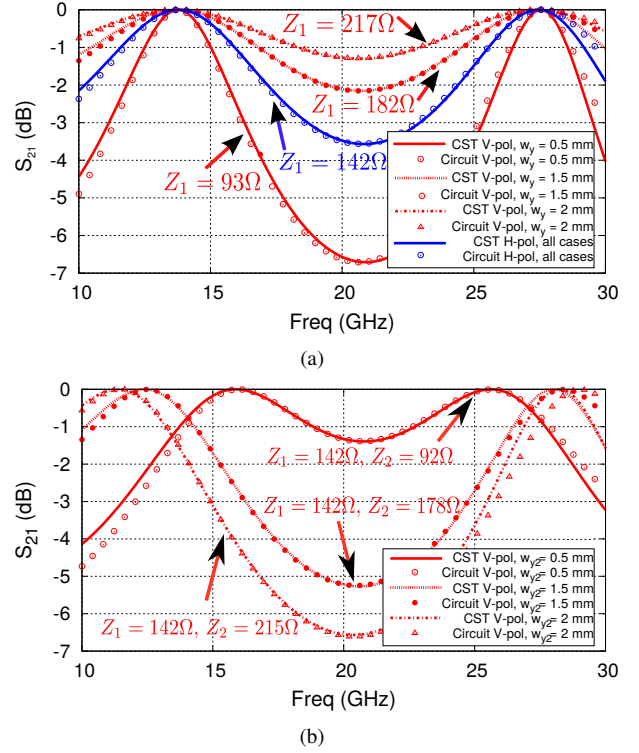


Fig. 4. (a)  $S_{21}$  for the unit-cell model in Fig. 2(a) considering V and H polarizations, and for different values of  $w_y$ . Structure parameters:  $p = 5.2$  mm,  $t = 0.4$  mm,  $d = 10.45$  mm,  $w_x = 1$  mm. (b)  $S_{21}$  for the unit-cell model in Fig. 2(b) under V-pol for different values of  $w_y$ . Structure parameters:  $p = 5.2$  mm,  $d_1 = 3.1$  mm,  $d_2 = 4.25$  mm,  $w_x = 1$  mm,  $w_y = 1$  mm.

approximately when  $d = \lambda/2$  and  $d = \lambda$ . This behavior is typical of transmission lines. Since the position of the two nulls is the same for any value of  $w_y$ , the propagation constant of the TEM mode can be regarded as independent from  $w_y$ , as it occurs with the TEM modes of a parallel-plate waveguide (where  $\beta = \omega/c$ ). The maximum value of the  $S_{11}$ -curves is sensitive to  $w_y$ , higher reflection values correspond to lower ones of  $w_y$ . This tendency is related to the decrease of the characteristic impedance in the equivalent circuit, and it is illustrated in the figure via dotted lines. The value of  $Z_1$  will approach that of the free-space impedance ( $Z_0$ ) as the width of the slit is increased. As it is intuitive to understand, when  $w_y$  increases, the matching between free space and the cell is improved (and perfect matching would appear when  $w_y = p$ ). The values provided by the equivalent circuit are plotted together with the full-wave simulations, showing very good agreement, and thus, proving the validity of the proposed simple model.

The results plotted in Fig. 3(b) show the evolution of the impedance of the TEM waveguide in terms of the ratio  $w_y/p$  (normalized slit width with respect to the periodicity). Such values have been obtained from the  $S_{11}$  provided by the full-wave solver. It can easily be demonstrated that  $Z_1 = Z_0 \sqrt{(1 + S_{11}) / (1 - S_{11})}$  at the frequency for which  $\beta d = \pi/4$ , with  $\beta = \omega/c$  being the propagation constant of the transmission line. Three different values of  $p$  are considered, and the curves are practically identical. It can be concluded that the control over the impedance can be obtained

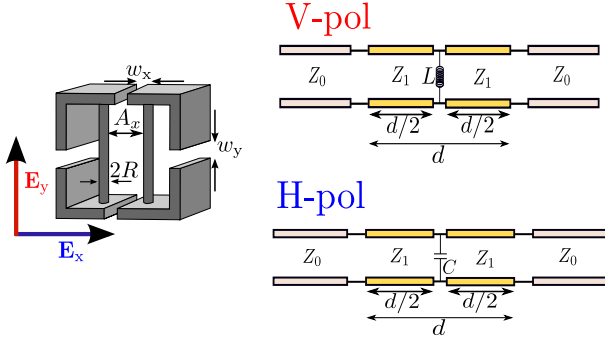


Fig. 5. TEM-cell including a couple of vertical columns which are defined by the geometrical parameters  $A_x$  and  $R$ . The circuit-model proposed for V and H-pol is also depicted.

by considering jointly the width of the slit normalized with respect to the periodicity (it is thus not necessary to specify both independent quantities). The same conclusions can be extracted considering the H-pol illumination, but modifying  $w_x$  rather than  $w_y$ .

The results in Fig. 4(a) consider a  $45^\circ$  slant plane-wave illumination on the cell of Fig. 2(a), which can be regarded as the in-phase excitation of simultaneous V- and H-pol. The results of  $S_{21}$  are plotted for different values of  $w_y$  impinging normally. It can be seen that the response for V-pol varies for each case, whereas H-pol has unchanged response. This confirms our previous assumption that the modification of  $w_y$  does not alter the scattering of H-pol, which is independent from  $w_y$ . As expected, the V-pol is highly sensitive to this parameter. The agreement between the circuit results and CST simulations is very good.

Finally, the stepped scenario described in Fig. 2(b) is considered in Fig. 4(b); its  $S_{21}$  is plotted for different values of  $w_{y2}$ . This figure shows that the stepping of the slit width allows to modify the relative position between the peaks of full-transmission that appeared at  $d = \lambda/2, d = \lambda$  in the previous uniform case. When  $w_{y1} \geq w_{y2}$  the peaks tend to approach to each other. This strategy will be used in the following sections to achieve wide-band transmission response from the cell.

The above examples corroborate that the proposed unit cell supports TEM dual-polarized modes. Additionally, the reduction of the problem to a circuitual framework is highly advantageous since the properties of transmission lines are well-known and simple to be applied. Typical techniques for bandwidth optimization based on transmission-line matching transformers could readily be employed if needed for a particular application.

### C. Introduction of loads and circuit representation

The previous TEM-cell is loaded with two identical metallic columns oriented along  $\hat{y}$ , which connect the top and bottom walls in the middle of the structure, as shown in Fig. 5. The columns are defined by a radius  $R$  and they are separated of a distance  $A_x$ . These loads are added with two main aims: allow for a means of phase manipulation of the transmitted fields (in

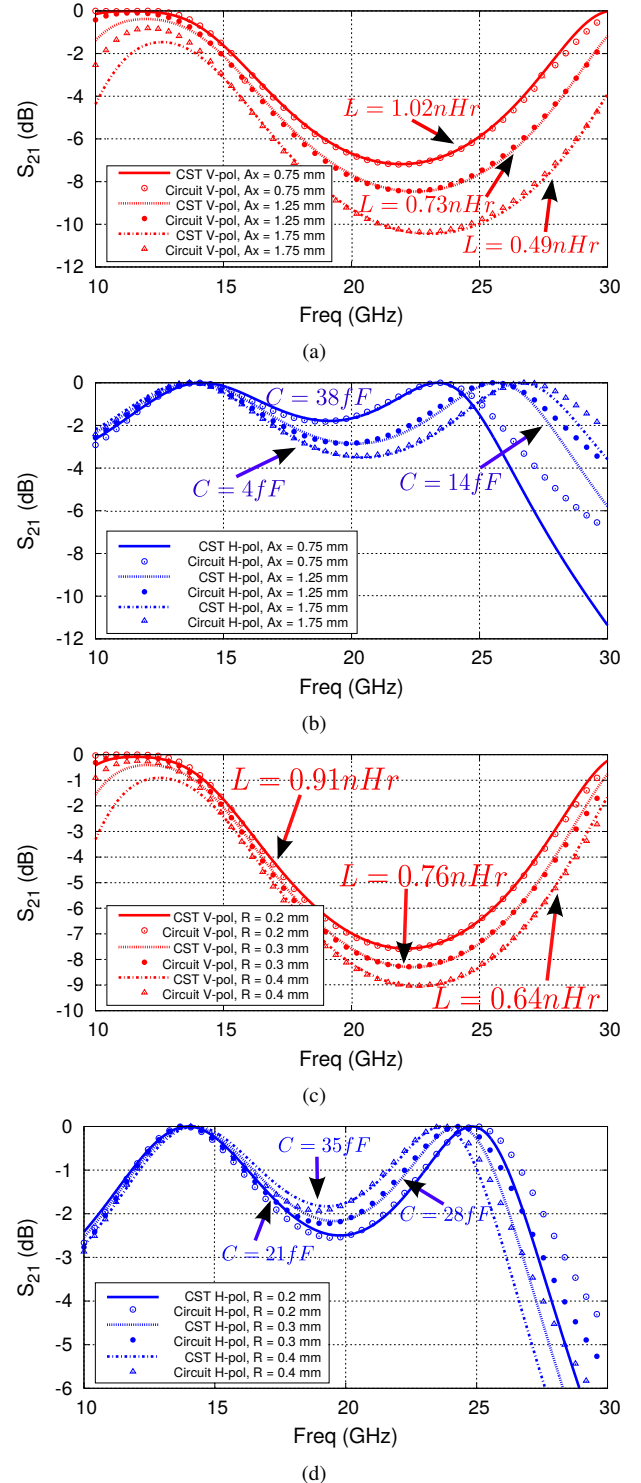


Fig. 6. Magnitude of  $S_{21}$  versus frequency for the cell in Fig. 5 under V and H-pol. (a/b) V/H-pol varying  $A_x$  for  $R = 0.22$  mm. (c/d) V/H-pol varying  $R$  for fixed  $A_x = 1$  mm. Structure dimensions are:  $p = 5.2$  mm,  $t = 0.4$  mm,  $w_y = 1$  mm,  $w_x = 1$  mm,  $d =$  mm.

order to induce polarization conversion), and enhance the cell robustness for prototyping.

In such a cell, the conditions encountered by V and H-pol incident fields are now different. The V-pol field, being parallel to the columns, mainly suffers an inductive opposition due to the excitation of an effective current which flows along them. On the contrary, for H-pol, the excited current is negligible since the electric field is perpendicular to the columns. Instead, effective charge is accumulated on the surface of the columns in this case, giving rise to a global capacitive contribution.

The duality associated to the columns can be easily analyzed from the equivalent circuit point of view. For the V-pol subproblem, the effect of the columns is globally magnetic, thus a regular inductance is the natural circuit element to account for them. Analogously, the H-pol subproblem includes a regular capacitance to describe the role of the columns. In the following, the numerical values of the equivalent inductance/capacitance are found by an easy numerical fitting with CST results. The columns dual-behavior breaks the previously identified independent control of the orthogonal impinging fields. Variations on the columns geometry now influence both polarizations simultaneously. However, the different nature of the lumped elements included in the circuit representation (inductance or capacitance) is well suited to the achievement of polarization conversion, as done in the case of meander-line gratings. In the following we analyze the impact of the columns in the magnitude and phase of the  $S_{21}$  of the cell, providing a comparison between CST simulations and the results of the proposed circuit model.

The magnitude of the  $S_{21}$  is analyzed in Fig. 6. V and H-pol are considered respectively in Fig. 6(a) and (b), where each of the different curves correspond to a different value of  $A_x$ . It can be seen that, as  $A_x$  increases, the corresponding values of inductance and capacitance decrease. The influence of this parameter is unequal for each polarization. V-pol is highly sensitive to  $A_x$  while H-pol is only slightly affected. Such unequal impact represents a valuable advantage for the design of a specific structure, since doing the optimization of the parameter  $A_x$  just for V-pol may be sufficient. The case of Fig. 6(c) and (d) illustrates the  $S_{21}$ -behavior, for V and H-pol respectively, considering fixed  $A_x$  and different values of  $R$ . The increase of  $R$  results in a reduction of the inductance value, while the equivalent capacitance experiences an increasing tendency, though the impact of  $R$  is still lesser comparing to the inductive case. The capacitance just varies from 21 to 35 fF, which is manifested by a difference lower than 1 dB between in their respective  $S_{21}$ -curves. It is worth mentioning that the agreement between results from CST and the circuit model is quite good in all cases, reinforcing the circuitual interpretation of the columns. From these results we can conclude that the distance between columns  $A_x$  is a more decisive parameter to control the amplitude of the cell  $S_{21}$ .

The impact of the columns geometry on the phase of the transmitted fields is often necessary for many applications, specially for those involving polarization conversion. The results in Fig. 7 show the phase of the  $S_{21}$  for two different values of  $A_x$  while keeping  $R$  fixed. It can be seen that the H-pol curves do almost overlap, confirming the almost negligible

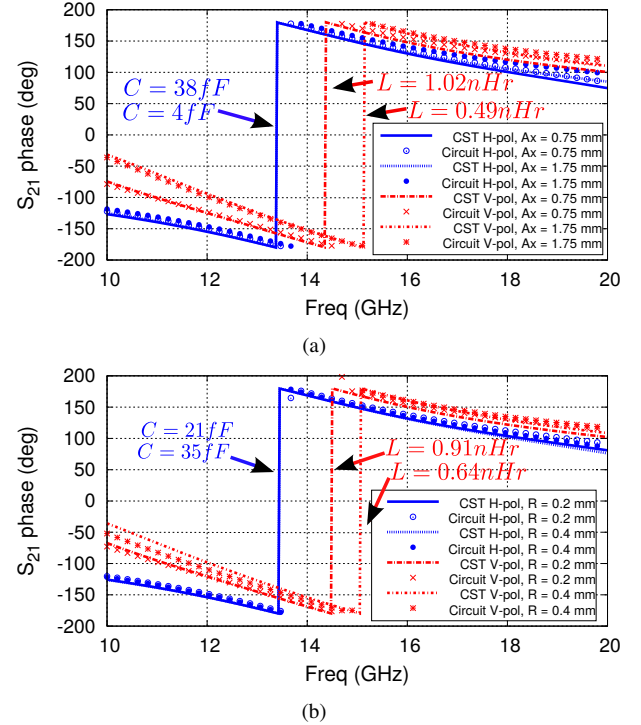


Fig. 7. Phase of  $S_{21}$  versus frequency for the structure in Fig. 6. (a) Variation of  $A_x$  with fixed  $R = 0.22$  mm. (b) Variation of  $R$  with fixed  $A_x = 1$  mm.

influence of the columns in the capacitive scenario that was observed before. For the inductive case (V-pol), the  $S_{21}$ -phase is significantly affected, manifesting a phase shift towards higher frequencies as  $A_x$  increases. Similar conclusions can be extracted from Fig. 7(b), where the impact of radius of the columns on the phase delay is considered. V-pol is influenced by the increment of  $R$ , whereas H-pol is not altered. As a conclusion, if a given phase shift between the V and H-pol is desired, it can be synthesized by tuning the phase of V-pol through the design of the columns geometry. The agreement between CST and the circuit model is very good.

A final study, considered in Fig. 8, is carried out to evaluate the interest in using a couple of columns loading the TEM-cell. The topology of the cell and the proposed equivalent circuit for V and H-pol are shown in Fig. 8(a). As it can be observed, each couple of columns is modelled by a single inductance/capacitance. The influence of the separation between the columns is again stronger for V-pol, as shown in Fig. 8(b) and (c). All the cell dimensions are considered fixed except for  $d_z$ . Both the magnitude and phase of the transmission coefficient for V-pol are highly impacted when the couples of columns move away or approach to each other. Wide band-pass transmission can be achieved for certain values of  $d_z$ . In this case, small disagreement is appreciated between CST and the circuit model. This difference is mainly due to the mutual coupling existing between both couples of columns, which is not taken into account in the circuit model. A more accurate model should include this coupling, at the cost of a significant complexity increase. Nevertheless, the current simple version of the circuit is sufficiently accurate to capture and understand the main electromagnetic phenomena

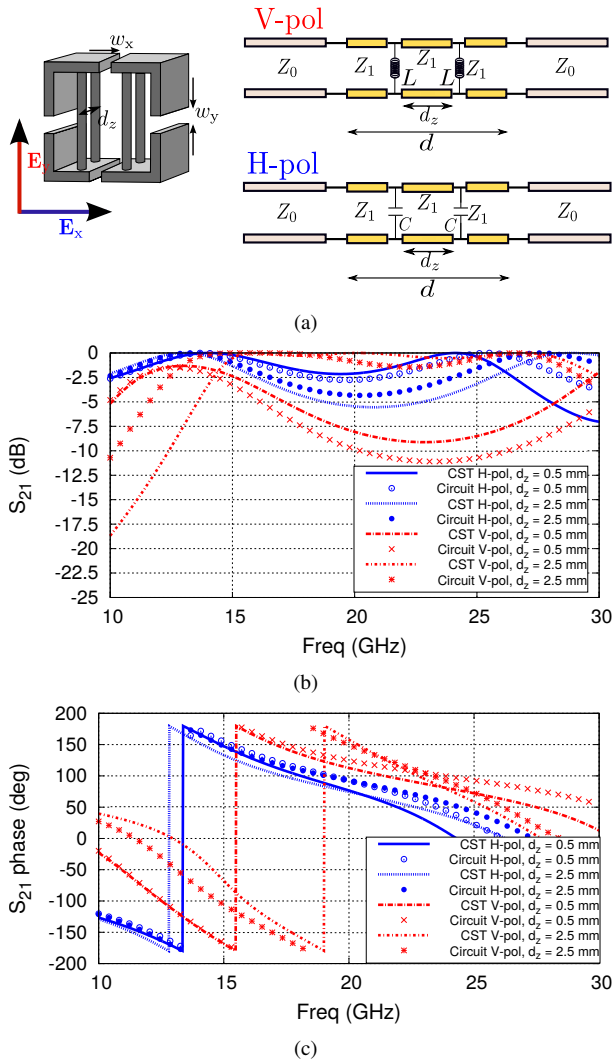


Fig. 8. (a) TEM-cell with two couples of columns: topology of the cell and equivalent circuit. The distance between these couples is defined by the parameter  $d_z$ . (b) Magnitude of  $S_{21}$  for V/H-pol. (c) Phase of  $S_{21}$  for V/H-pol. Structure dimensions are  $p = 5.2$  mm,  $t = 0.4$  mm,  $w_y = 1$  mm,  $w_x = 1$  mm,  $d = 10.45$  mm,  $A_x = 1$  mm,  $R = 0.22$  mm.

appearing in the structure, predict them numerically and it allows to be easily used for design purposes.

### III. DESIGN OF CP POLARIZERS WITH TEM-CELL

The properties of the TEM-cell can be used to design polarizing screens converting a 45-degree-slant linearly-polarized wave into a circularly polarized one. In the following sections, a preliminary design is firstly presented together with a methodology based on the circuit model. Later, the design is finalized by applying some structural modifications that allow for SLM manufacturing. It should be noted that this is the first time that a co-design procedure is adopted in order to perform RF design of periodic structure to be well suited to be 3D-printed in metal.

#### A. Preliminary design

The unit-cell in Fig. 9 is proposed to conceive a polarizing screen. Such a configuration includes a uniform slit in the

lateral walls, a stepped slit in the top/bottom walls and two couples of columns inside. The incident electric field is  $\pm 45^\circ$ -slanted with respect to the  $x$ -axis, and it can be decomposed into two sub-problems involving equal in-phase excitation of V and H-pols. These sub-problems can be modeled by the circuits proposed in Fig. 10, that are based on the developments presented in the previous section. The circuit model for V-pol shown in Fig. 10(a) is defined by the following main parameters: the impedance  $Z_1$  (related to the normalized slit  $w_y/p$ ), the inductances  $L$  (that characterize the vertical columns), the distance  $d_z$  (longitudinal separation between couples of columns) and the length  $d$  (total longitudinal thickness of the cell). The circuit model for H-pol includes additional transmission-line sections that represent the stepped sections of the top and bottom slits. In this case, the slit is symmetrically split into 3 sections, whose width is  $w_{x1}/p$  in the input and output of the cell, and  $w_{x2}$  in the middle. This corresponds to a cascade of transmission-line sections with characteristic impedance  $Z_1$  and  $Z_2$ , as shown in Fig. 10(b). The presence of the columns is now represented by the capacitances  $C$ .

The methodology that is proposed to design a polarizing cell is next explained, and based on the previous circuit models. A look-up table is built relating the evolution of each of the circuit parameters in terms of the variation of its corresponding geometrical element. For example, the evolution of the value of the inductance in terms of the radius of the columns. Employing these tables, an optimization process is performed basing on two steps. Firstly, the V-pol wide band-pass transmission is firstly synthesized, by choosing the parameters  $Z_1$ ,  $d_1$ ,  $d_2$  and  $L$ . Then the elements controlling the H-pol are designed, namely  $Z_1$ ,  $Z_2$ ,  $d_2$  and  $d_3$ . In this second step, the goals for this optimization are high transmission in the band of interest and also phase quadrature with respect to the phase of V-pol. It should be noted that this second step takes into account the position of the phase curve obtained for V-pol, with the aim of pursuing the  $90^\circ$ -degrees difference. It should be highlighted that such a design methodology is very simple, and this has been made possible by the circuitual reasoning employed when building progressively the 3-D unit cell.

The performance of a cell designed for operation both in the K- and Ka-bands is shown in Fig. 11 (thus covering from 18 to 30 GHz). The scattering parameters are plotted versus frequency for V and H-pol, both in magnitude and phase. Results obtained by the circuit model are compared to those provided by CST in order to check the validity of our predictions. The magnitude of the transmission coefficient is plotted in terms of the insertion losses in Fig. 11(a), where a broad-band response covering the desired frequency band and with small ripple is observed. The phase of the transmission coefficient is plotted in Fig. 11(b), showing an almost linear variation along the whole band for both polarizations. The black curve represents the phase shift between both components, and it keeps almost constant around  $90^\circ$ . It can thus be inferred that this structure behaves as a polarization converter in the band of interest.

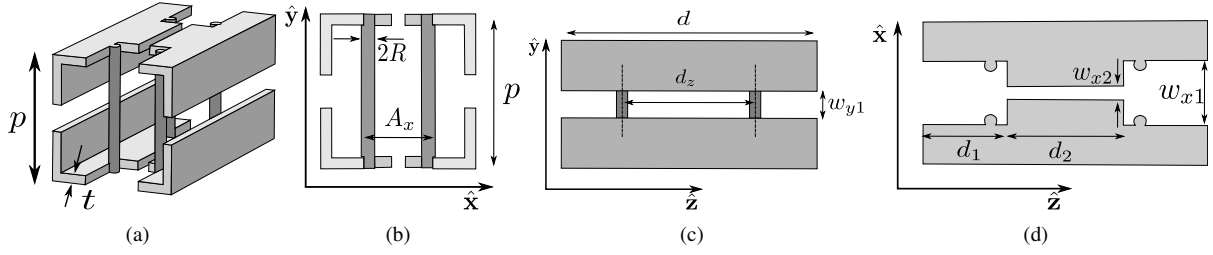


Fig. 9. Proposed TEM-cell for synthesizing linear-to-circular polarization conversion. The cell is illuminated by a 45-degree-slant linearly-polarized plane wave. (a) 3D-view, (b) XY-plane, (c) YZ-plane, (d) XZ-plane.

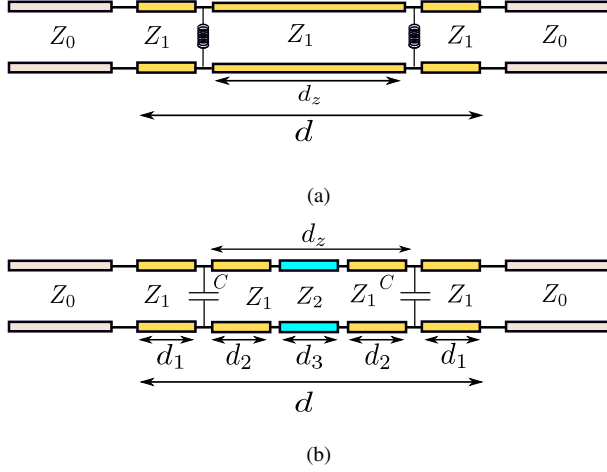


Fig. 10. (a) Equivalent circuit for V-pol and for (b) H-pol, associated to the cell in Fig. 9.

### B. Modifications for SLM-printing

The 3D geometry of the conceived polarizer encourages its prototyping via modern 3D-printing techniques. In our case, since the structure is full-metal, we can envision to use metallic powder as the building material, basing on the technique of SLM. This 3D-printing technique is the typically preferred process for hardware prototyping in the space industry, since it allows to have a raw manufactured part that can already meet the typical associated mechanical and thermal requirements [37], [40]. The tolerances associated to SLM depend on the type of metal powder that is employed, and the orientation of the piece inside the 3D-printer and they can vary between 50  $\mu\text{m}$  and 150  $\mu\text{m}$ . In principle, in order to obtain the best results, the structure should be vertically printed and self-supported (thus, not presenting unsupported overhanging faces or abrupt appearance of long parts). To avoid the printing of undesired supports, it can also be foreseen to 3D-print the piece under a certain angle, but this leads to deterioration of the manufacturing tolerances as a consequence of the staircase effect [38], [39]. It should be noted that this is the first development in the literature that proposes periodic screens that can be printed vertically.

To foresee successful SLM manufacturing of the cell in Fig. 9(a), the chosen printing direction is the  $z$  axis. Such vertical printing of the piece implies two structural modifications. The resulting modified version is depicted in Fig. 12.

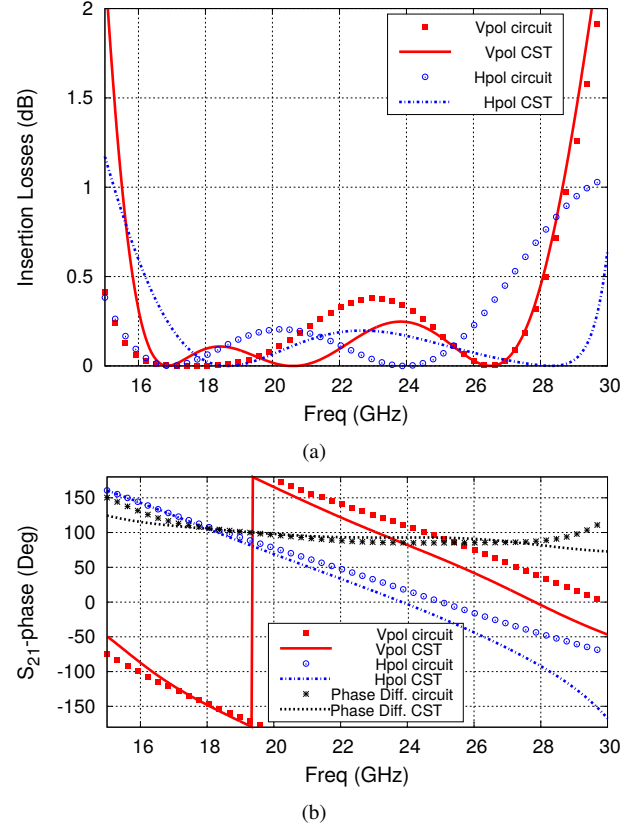


Fig. 11. Performance of the designed polarizing cell for both V and H-pol: (a) Insertion losses, (b) phase of the  $S_{21}$  transmission coefficient. Results from the circuit model and CST are plotted. Structure dimensions are  $p = 5.2$  mm,  $t = 0.4$  mm,  $w_{y1} = 1.12$  mm,  $w_{x1} = 2.33$  mm,  $w_{x2} = 0.47$  mm,  $d = 10.45$  mm,  $d_2 = 4.4$  mm,  $d_z = 5.7$  mm,  $A_x = 2.05$  mm,  $R = 0.22$  mm.

Firstly, a rectangular post of thickness  $g$  is included at the input of the cell, which is perpendicular to  $z$  and parallel to the diagonal axis of the cell (inclined of  $45^\circ$  with respect to  $x$ ). This post provides mechanical robustness to the cell and it does not present any supporting restriction, since it is directly built over the base plate of the printer. The presence of this post barely affects the performance of the original cell, but it reduces the freedom to excite it. In fact, the original cell of Fig. 9 allows to be illuminated by  $\pm 45^\circ$ -slant electric fields, giving rise to transmitted circularly polarized signals with orthogonal sense of rotation. In the modified version of the cell, the illuminating field must be perpendicular to the post orientation (as illustrated by the vector  $E_{\text{inc}}$  in Fig. 12(a)). This way, it is assured that the post will be almost transparent to

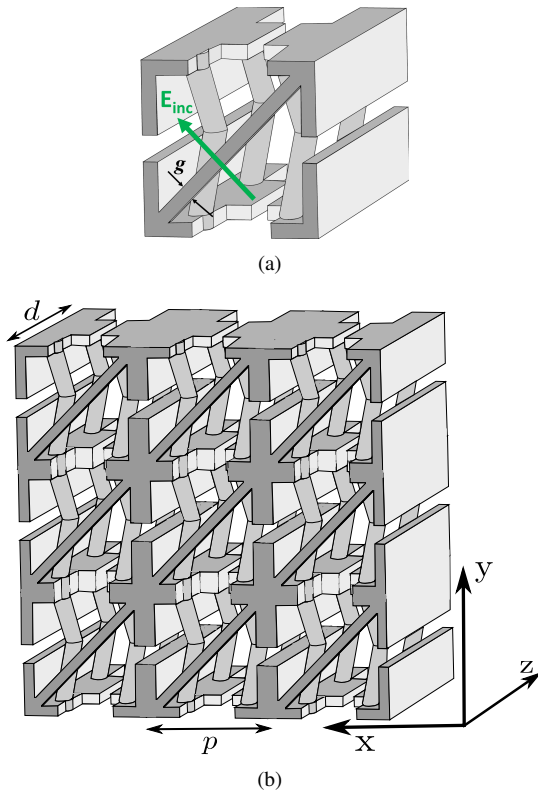


Fig. 12. Modified version of the cell in Fig. 9 in order to match the requirements of SLM 3D-printing. A rectangular post of thickness  $g$  is added at the input of the cell. This post is inclined of  $45^\circ$  with respect to  $x$  and perpendicular to  $z$ . (a) Single cell with detail of the orientation of the illuminating field. (b) Example of  $3 \times 3$  array.

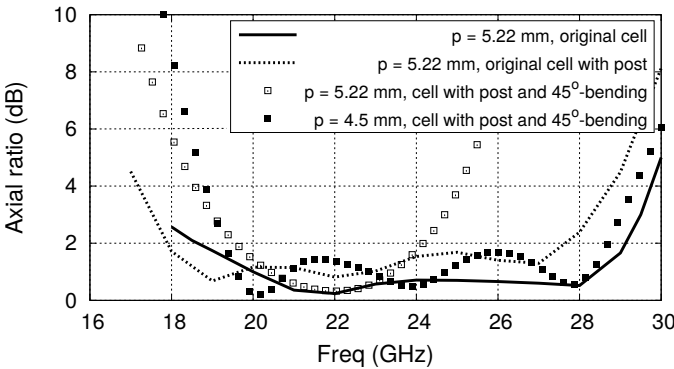


Fig. 13. AR versus frequency for different versions of the polarizing unit cell. Re-design of the cell in order to recover broad-band operation after performing the modifications for SLM printing. The structure dimensions of the cases with  $p = 5.22$  mm are identical. For the case with  $p = 4.5$  mm the structure dimensions are the following:  $t = 0.4$  mm,  $w_{y1} = 0.76$  mm,  $w_{x1} = 1.86$  mm,  $w_{x2} = 0.45$  mm,  $d = 10.45$  mm,  $d_2 = 4.7$  mm,  $d_z = 5.4$  mm,  $A_x = 1.86$  mm,  $R = 0.25$  mm and  $g = 0.5$  mm.

the impinging field. The impact of the presence of the post can be analyzed in Fig. 13, which shows the axial ratio (AR) of the original cell without and with the post (the latter labelled as *original cell with post* in the legend). It can be appreciated that a small shift towards lower frequencies appears in the AR curve, but its level remains below 2 dB. An impinging electric field whose polarization is parallel to the post will be strongly reflected backwards, experiencing almost an electric

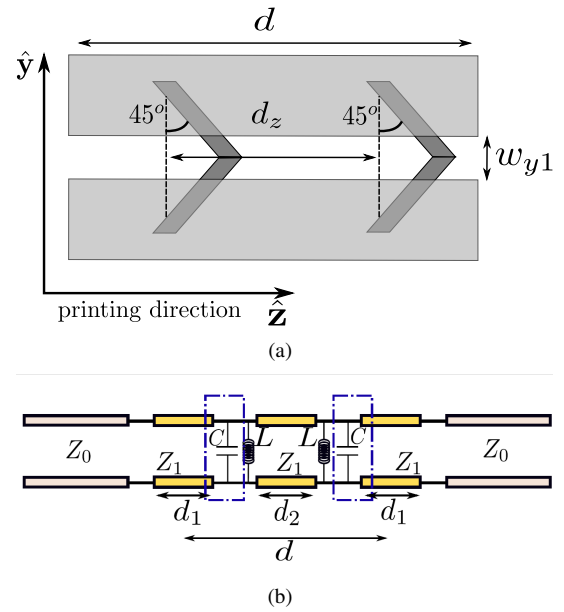


Fig. 14. Inclination of the columns inside the unit-cell along the printing direction (the  $z$  axis). (a) Lateral view of the columns inside the cell, illustrating their longitudinal bending for self-supported 3D-printing. An isosceles triangle of  $45^\circ$  is formed. (b) Modified equivalent circuit proposed for V-pol, including a parallel capacitive contribution associated to the bending.

wall boundary condition. This scenario is thus not considered. It is worth noting that, other mechanical strategies can be envisioned in order to maintain the dual-polarized character of the structure, for example adding a frame around the screen and removing the post. This would require a dedicated mechanical design that guarantees robustness (including an assessment of the deformations). Since this is the first prototype of this kind ever done, such a mechanical study has not been considered yet.

The second action taken to match the guidelines of SLM printing is the inclination applied to the columns. In fact, large-sized elements perpendicular to the printing direction are not self-supported, and there exists a high risk of deformation and breaking. Such inclination is shown in Fig. 12, which makes the column appear progressively and be built vertically by the printer smoothly as it advances on the  $z$  direction. As a result, the columns are bent with respect to their middle point in height. Their lateral geometry can be observed in Fig. 14(a), which shows that an isosceles triangular-shape geometry is pursued, where both identical vertices have  $45^\circ$  (this is the minimum value to ensure successful manufacturing). The electromagnetic response of the cell is impacted by this modification, as shown in Fig. 13 (see the curve labelled as  $p=5.22$  mm, cell with post and  $45^\circ$  bending). The AR bandwidth is now narrower, this is mainly because the V-pol is affected by the bending of the columns. Under this polarization, the columns are no longer seen as single parallel inductances. As illustrated in Fig. 14(a), a small capacitive contribution is created between the edges of the bent columns, which is now included in the modified version of the circuit in Fig. 14(b). On the contrary, the H-pol is very little affected, and its corresponding circuit topology in Fig. 10(b) is still valid. Note that this new scenario is again accurately characterized

by the proposed circuits, though this validation is not included here for the sake of conciseness.

The circuit in Fig. 14(b) allows to identify the way to compensate for the parasitic capacitance brought by the bent columns. In fact, an almost inductive behavior can be experienced if the resonance of the  $LC$  circuits is shifted towards higher frequencies. This can be achieved by reducing the periodicity of the cell. Such a strategy has been applied and the broad-band AR performance is recovered, as proven in Fig. 13 (see curve labelled  $p=4.5$  mm, cell with post and  $45^\circ$  bending). It should be noted that the reduction of the periodicity launches again the design process. Basically, as explained previously, the ratio between the slit width and the periodicity  $w/p$  must be maintained. In this sense, lowering  $p$  is accompanied by a convenient decrease in  $w_{x,y}$ . When  $p = 4.5$  mm the performance associated with the original cell is achieved (with minor differences), as shown in Fig. 13. The new geometrical dimensions appear in the caption.

#### IV. EXPERIMENTAL RESULTS

The co-design approach adopted in the previous section (design for additive manufacturing) gives rise to a geometry of polarizer that can be 3D-printed straightforward basing on SLM. In spite of all the advantages associated to metal additive manufacturing, SLM presents a significant disadvantage when comparing to classical machining, related to its surface roughness. This may result in high insertion losses when operating above the Ku-band, even if a material with high bulk conductivity is used [38]. In particular, the conceived cells are printed employing Titanium. Such material is chosen for providing high precision. Lower tolerances can be attained in comparison to the ones associated to Aluminium alloys (which is the common choice in RF 3D-printed hardware), since the grain of the metal powder is the smaller. When choosing such a material, a trade-off is made between precision and conductivity. In fact, the disadvantage of using Titanium is that its conductivity is not as high as in Aluminium or Copper, which will result in higher insertion losses. However, our decision has been encouraged by the fact that the surface conductivity can be further improved by post-processing of the raw printed piece, while the tolerances can not be improved after printing. The present prototype has been treated to reduce surface roughness with application of sandblasting. Recent publications illustrate the improvement brought by electroless copper plating considering different RF devices [41], [42].

The polarizer design explained in the previous section is validated experimentally. The 3D-printed samples are produced by our industrial partner *Thales 3D Morocco*, and they are shown in Fig. 15. The measurement of the prototypes has been done in a commercial quasi-optical system that allows to rigorously emulate plane-wave illumination; it is shown in Fig. 16 [43]. The test setup frequency band goes from 18 to 32 GHz. This range is covered in two consecutive intervals, employing two couples of TX-RX corrugated horns that operate respectively from 18 to 26 GHz, and from 26 to 32 GHz. The device under test (DUT) is placed in the middle of the system, and it consists of a rectangular support

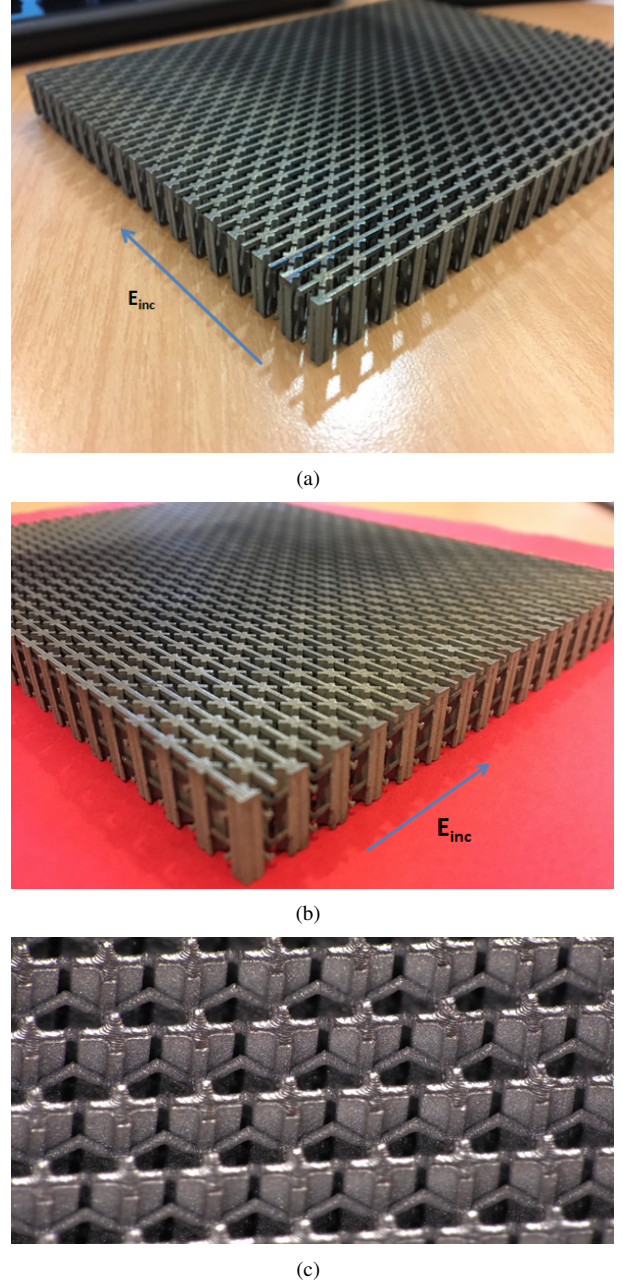
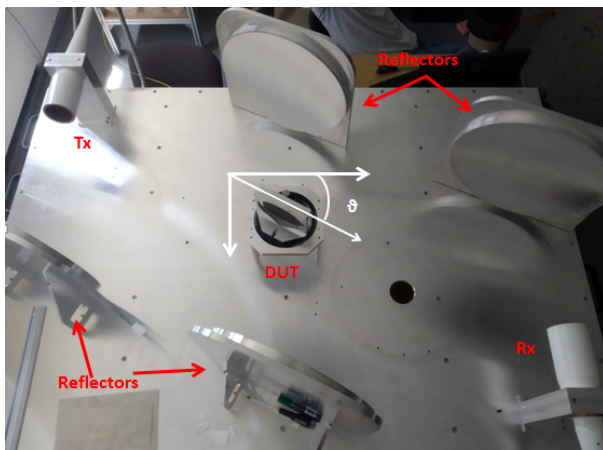


Fig. 15. SLM prototypes. (a) Polarizer #1, for TE incidence. (b) Polarizer #2, for TM incidence. (c) Zoomed image of one of the prototypes where the column-bending can be appreciated.

with an elliptical hole that holds the polarizer, as it is shown in Fig. 16(b). The reflectors in the system focus the radiation from the horns creating a Gaussian beam with planar phase front at the position of the DUT [43]. The couple of TX-RX horns is connected to a VNA (Keysight N5227A) in order to obtain the S parameters of the DUT. As it is sketched in Fig. 16(a), oblique incidence can be attained by rotating the DUT in the center of the setup. Such rotation can only be done with respect to a single axis (the one perpendicular to the table plane).

Two different prototypes have been fabricated, they are named as #1 and #2 and they are shown in Fig. 15(a) and (b). They are rectangular arrays of unit cells and they can



(a)

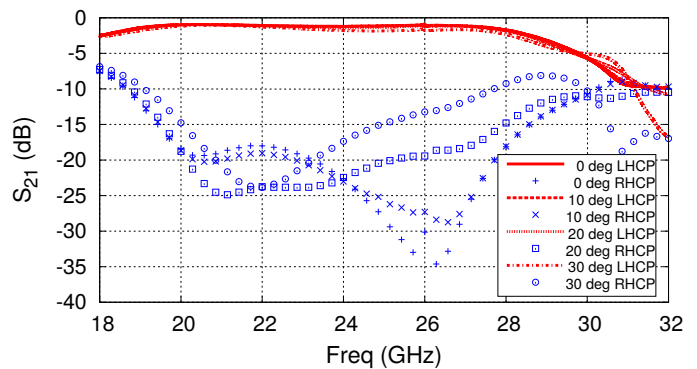


(b)

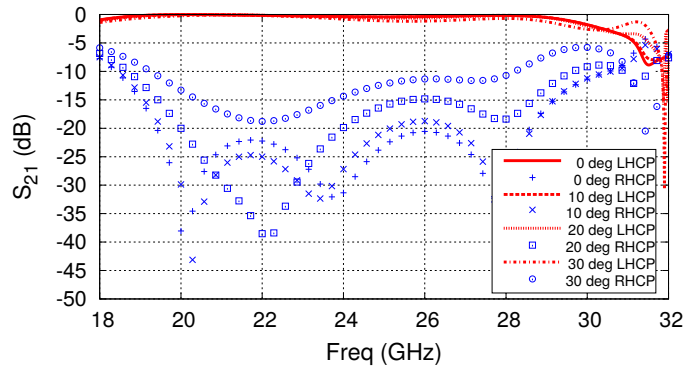
Fig. 16. (a) IETR experimental setup based on a quasi-optical system. (b) DUT, including the support and the polarizer.

be sandwiched within the setup support as shown in Fig. 16(b). Both samples consider exactly the same design of unit-cell, but one array is rotated of  $90^\circ$  with respect to the other one. They will be used to characterize either the TE or TM incidence. The need for these two prototypes is due to the single axis rotation allowed by the experimental setup. In order to measure the performance of the polarizer, V-pol and H-pol are characterized one after the other and combined afterwards in post-processing. Therefore, when the DUT is rotated, TE and TM incidences are emulated by considering either the V-pol or H-pol radiation from the TX horn. Prototypes #1 and #2 have been manufactured to be used respectively in those two scenarios. Finally, it should be noted that instead of applying a  $45^\circ$ -slant to the field illuminating the polarizer, the cells are turned of  $45^\circ$  in the manufactured prototypes (this is strictly equivalent for the polarization conversion, but it simplifies the measurement). A zoom of one of the polarizers is shown in Fig. 15(c) in order to appreciate the details of the cells and the bending of the columns.

The performance of the polarizer under TE incidence is analyzed in Fig. 17. The transmission coefficient is plotted, both in right-handed and left-handed CP ( $S_{21}^{\text{RHCP}}$  and  $S_{21}^{\text{LHCP}}$ ), and considering incidences from normal up to  $30^\circ$ . These

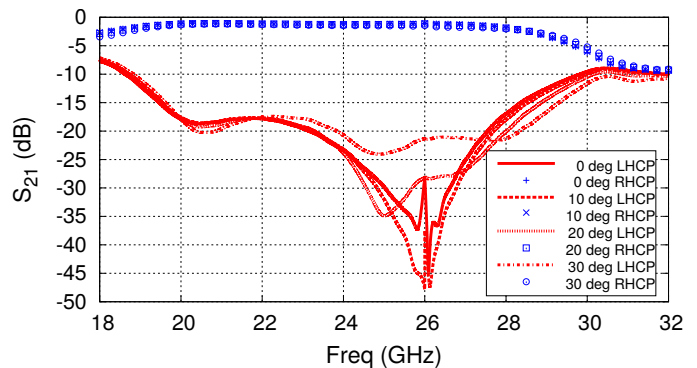


(a)

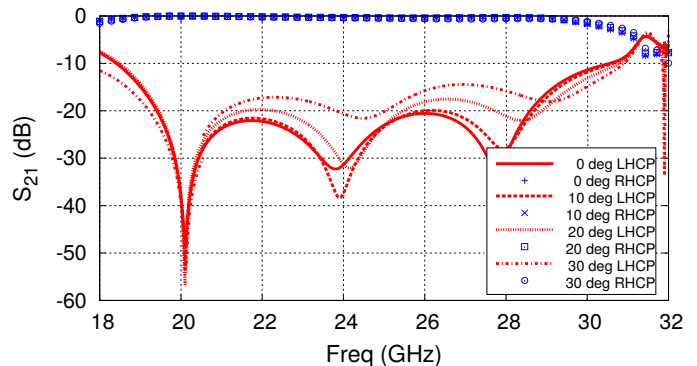


(b)

Fig. 17.  $S_{21}$  for TE incidences from  $\theta = 0^\circ$  to  $30^\circ$ . (a) Experimental results. The glitch appearing at 26 GHz is related to the change of horns in the quasi-optical setup. (b) CST simulations.



(a)



(b)

Fig. 18.  $S_{21}$  for TM incidences from  $\theta = 0^\circ$  to  $30^\circ$ . (a) Experimental results. The glitch appearing at 26 GHz is related to the change of horns in the quasi-optical setup. (b) CST simulations.

coefficients provide both information about the purity of circular polarization and the insertion losses. The results obtained experimentally are directly shown in Fig. 17(a), which can be compared to those plotted in Fig. 17(b), that are extracted from CST. High transmission is observed that is LHCP, and very good agreement between both figures. The cross-pol discrimination can be defined in this case as  $XPD = |S_{21}^{LHCP}/S_{21}^{RHCP}|$ . It can be observed that the XPD is better than 15 dB from 19.5 GHz up to 28.6 GHz for normal incidence, corresponding to a 37.8 % bandwidth. This value deteriorates as the angle of incidence increases, resulting in a 22.2% bandwidth for the same XPD level (from 20 GHz to 25 GHz) at 30°-incidence. Note that the threshold of  $XPD = 15$  dB corresponds to an axial-ratio value of 3 dB [44], thus representing a polarization conversion of good quality.

Analogously, Fig. 18 shows the transmission coefficient under TM incidence up to 30°. Now, RHCP conversion is achieved. As it was previously mentioned, prototype #2 is now employed since the incident electric field points along  $x$ . The electric field direction (opposite to that impinging on prototype #1 in the previous case) is responsible of the change of the rotation sense of the polarization vector of the outgoing field. XPD levels better than 15 dB are again obtained between 19.5 GHz and 28.6 GHz (37.8 % bandwidth). In contrast to the TE case, the TM scenario is found to be more stable with the angle of incidence and the XPD bandwidth is not reduced for incidences up to 30°.

The insertion losses were expected to be lower than 0.5 dB in the operation bandwidth (see Fig. 11(a)). However, it can be observed in the measurements that the value of  $S_{21}$  for the co-pol keeps between 1 and 1.2 dB both for TE and TM incidences. Several reasons justify this different value. The first one was introduced at the beginning of the section, and it is the real conductivity of the Titanium alloy (which differs from the bulk one and is yet unknown). Such conductivity will result in an increase of the polarizer losses. The second one is associated to the limitations of the experimental setup. In fact, the absence of an OMT at the TX horn prevents the measurement of the cross-polarization that may be reflected backwards by the DUT. Secondly, it can only be measured the transmission through the DUT in the same direction as the impinging field. The specular reflection can not be measured, for example. It is therefore not possible to assess which amount of the  $S_{21}$  level is directly related to the insertion losses of the device or to the limitations of the measurement setup. In fact, we can not evaluate if there is propagation of energy in other directions (due to the eventual appearance of small asymmetries in the prototype or misalignment in the quasi-optical setup). A possible extension of this work could consider the post-processing of the SLM piece, for example, reducing roughness and improving surface conductivity by applying chemical blasting and metal plating afterwards.

It should be noted that the polarizer was designed considering normal incidence, but that its behavior has not been drastically deteriorated when increasing it to 30°. This opens the way for further designs where the angle of incidence is already included in the design process, giving rise to more complex 3D geometries of the elements loading the TEM-

cells.

Finally, it can be concluded that the agreement between the measurements and the theoretical predictions is very good, which proves the great bandwidth enhancement allowed by the original TEM-cell, and the great potential of the concept. The success of the experimental campaign also points out the need for a co-design approach involving steps of RF-design considering the specificity of additive manufacturing.

## V. CONCLUSION

This paper proposes a novel concept to conceive full-metal polarizers based on 3D periodic structures. The original unit-cell is broadband because it exploits the propagation of the TEM modes, contrary to previous designs based on resonating elements. The mechanical robustness of the cell is guaranteed thanks to the inclusion of metallic columns, that have also an RF functionality, since they are conveniently designed to keep the broad pass-band of the structure and to force linear-to-circular polarization conversion. The behavior of the cell and its design is supported by the use of an equivalent circuit. The circuital characterization of the cells has reduced considerably the optimization process. A co-design approach is employed that considers additive manufacturing through SLM. This approach has enabled a successful experimental campaign, that validates the broad-band polarization conversion not only for normal incidence but also for angles reaching 30°.

## ACKNOWLEDGMENTS

The authors would like to thank Dr. L. Le Coq and F. Boutet from IETR, for their help in the experimental activities.

## REFERENCES

- [1] X. Huang, C. Yang, Z. Lu, and P. Liu, "A novel frequency selective structure with quasi-elliptic bandpass response," in *IEEE Antennas Wireless Propag. Lett.*, vol. 11, pp. 1497–1500, 2012.
- [2] W. Tang, J. Zhu, C. Wang, J. Ge, Z. Yu and W. Zhuang, "Waveguide 3D FSSs with 3D-printing technique," in *2016 International Conference on Electromagnetics in Advance Applications (ICEAA)*, vol. 1, pp. 675–678, Cairns (Canada), Sept. 2016.
- [3] J. Zhu, W. Tang, C. Wang, C. Huang, and Y. Shi, "Dual-polarized bandpass frequency-selective surface with quasi-elliptic response based on square coaxial waveguide," in *IEEE Trans. Antennas Propag.*, vol. 66, no. 3, pp. 1331–1339, March 2018.
- [4] C. Pelletti, G. Bianconi, R. Mittra and Z. Shen, "Frequency selective surface with wideband quasi-elliptic bandpass response," in *Electronic Letters*, vol. 49, no. 17, pp. 1052–1053, Aug. 2013.
- [5] B. Liang, and M. Bai, "Subwavelength three-dimensional frequency selective based on surface wave tunneling," in *Optics Express*, vol. 24, no. 13, pp. 14679–14702, June 2016.
- [6] W. Zhang, B. Li, L. Zhu, Y. Han, and Y. Liu, "3D novel passband frequency selective structures based on stacked planar slotlines: modeling, desing and validation," in *Proceedings on 2018 Asia-Pacific Microwave Conference*, vol. 1, pp. 1277–1279, Kyoto, Japan, Aug. 2017.
- [7] B. Sanz-Izquierdo, and E. A. Parker, "3D printing of elements in frequency selective arrays," in *IEEE Trans. Antennas Propag.*, vol. 62, no. 12, pp. 6060–6066, Dec. 2014.
- [8] D. Z. Zhu, M. D. Gregory, P. L. Werner and D. H. Werner, "fabrication and characterization of multiband polarization independent 3-D-printed frequency selective structures with ultrawide fields of view," in *IEEE Trans. Antennas Propag.*, vol. 66, no. 11, pp. 6096–6105, Nov. 2018.
- [9] W. Wang, Q. Cao, and Y. Zheng, "Bandstop frequency selective structures based on stepped-impedance loop resonators: design, analysis and measurements," in *IEEE Trans. Antennas Propag.*, vol. 67, no. 2, pp. 1053–1064, Feb. 2019.

- [10] A. A. Omar, and Z. Shen, "Multiband high-order bandstop 3D frequency-selective structures," in *IEEE Trans. Antennas Propag.*, vol. 64, no. 6, pp. 2217–2226, June 2016.
- [11] A. K. Rashid, Z. Shen, and S. Aditya, "Wideband microwave absorber based on a two-dimensional periodic array of microstrip lines," in *IEEE Trans. Antennas Propag.*, vol. 58, no. 12, pp. 3913–3922, Dec. 2010.
- [12] Y. Yu, G. Q. Luo, A. O. Ahmed, X. Liu, W. Yu, Z. Cheng, and Z. Shen, "3D absorptive frequency-selective reflection and transmission structures with dual absorption band," in *IEEE Access*, pp. 72880–72888, Nov. 2018.
- [13] G. Q. Luo, W. Yu, Y. Yu, X. H. Zhang and Z. Shen, "A three-dimensional design of ultra-wideband microwave absorbers," in *IEEE Trans. Antennas Propag.*, vol. 68, no. 10, pp. 4206–4215, Oct. 2020.
- [14] R. Kronberger, and P. Soboll, "New 3D printed microwave metamaterial absorbers with conductive printing materials," in *Proceedings of the 46<sup>th</sup> European Microwave Conference (EuMC 2016)*, vol. 1, pp. 596–599, London, United Kingdom, Oct. 2016.
- [15] T. Deng, Y. Yu, Z. Shen, and Z. N. Chen, "Design of 3-D multi-layer ferrite-loaded frequency-selective rasorbers with wide absorption bands," in *IEEE Trans. Antennas Propag.*, vol. 67, no. 1, pp. 108–117, June 2019.
- [16] I. M. Ehrenberg, S. E. Sarma, and B. Wu, "A three-dimensional self supporting low-loss microwave lens with a negative refractive index," in *journal Applied Physics*, vol. 112, pp. 073114 1–4, July 2012.
- [17] A. Shastri et al., "3D Printing of Millimetre Wave and Low-Terahertz Frequency Selective Surfaces Using Aerosol Jet Technology," in *IEEE Access*, vol. 8, pp. 177341–177350, 2020.
- [18] Qiu, Shihao and Guo, Qingxin and Li, Zengrui "Tunable Frequency Selective Surface Based on a Sliding 3D-Printed Inserted Dielectric" in *IEEE Access*, vol. 9, 2021.
- [19] A. A. Omar, W. Hong, A. A. Awamry, and A. Mahmoud, "A single-layer vialess wideband reflective polarization rotator utilizing perforating holes," in *IEEE Antennas Wireless Propag. Lett.*, vol. 19, no. 2, pp. 2053–2056, Dec. 2020.
- [20] K. X. Wang, and H. Wong, "A wideband millimeter-wave circularly polarized antenna with 3D printed polarizer," in *IEEE Transactions on Antennas and Propagation*, vol. 65, no. 3, pp. 1038–1046, March 2017.
- [21] C. Ding, and K. Luk, "Wideband high-gain circularly polarized antenna using artificial anisotropic polarizer," in *IEEE Trans. Antennas Propag.*, vol. 67, no. 10, pp. 6645–6649, Oct. 2019.
- [22] H. Li, B. Li, and L. Zhu, "Wideband linear-to-circular polarizer based on orthogonally inserted slot-line structures," in *IEEE Antennas Wireless Propag. Lett.*, vol. 18, no. 6, pp. 1169–1173, Jun 2019.
- [23] C. Molero, and M. García-Vigueras, "Circuit modeling of 3-D cells to design versatile full-metal polarizers," in *IEEE Trans. microw. Theory Techn.*, vol. 67, no. 4, pp. 1357–1369, March 2019.
- [24] C. Molero, E. Menargues, and M. García-Vigueras, "All metal 3D frequency-selective surface with versatile dual-band polarization conversion," in *IEEE Trans. Antennas Propag.*, vol. 68, no. 7, pp. 5431–5441, July 2020.
- [25] L. Young, L. Robinson, and C. Hacking, "Meander-line polarizer," in *IEEE Trans. Antennas Propag.*, vol. 21, no. 3, pp. 376–378, May 1973.
- [26] R. Chu, and K. Lee, "Analytical model for a multilayered meander-line polarizer plate with normal and oblique plane-wave incidence," in *IEEE Trans. Antennas Propag.*, vol. 35, no. 6, pp. 652–661, June 1987.
- [27] M. Letizia, B. Fuchs, C. Zorraquino, J. F. Surcher, and J. R. Mosig, "Oblique incidence design of meander-line polarizers for dielectric lens antennas," in *Progress in Electromagnetics Research B*, vol. 45, pp. 309–335, Nov. 2012.
- [28] E. Arnaud, R. Chantalat, M. Koubeissi, T. Monediere, E. Rodes and M. Thevenot, "Global design of an EGB antenna and meander-line polarizer for circular polarization," in *IEEE Antennas Wireless Propag. Lett.*, vol. 9, pp. 215–218, March 2010.
- [29] M. A. Joyal, and J. J. Laurin, "Analysis and design of thin circular polarizers based on meander lines," in *IEEE Trans. Antennas Propag.*, vol. 60, no. 6, pp. 3007–3011, June 2012.
- [30] M. A. Joyal, M. Riel, Y. Demers, and J. J. Laurin, "A meander-line circular polarizer optimized for oblique incidence," in *IEEE Trans. Antennas Propag.*, vol. 63, no. 12, pp. 5391–5398, Dec. 2015.
- [31] M. A. Joyal, and J. J. Laurin, "Design and analysis of a cascade of circular polarization frequency selective surface at Ka band," in *IEEE Trans. Antennas Propag.*, vol. 62, no. 6, pp. 3043–3053, June 2014.
- [32] E. Doumanis, G. Goussetis, R. Cahill, V. Fusco, and H. Legay, "Dual frequency polarized surfaces for Ka-band applications," in *6<sup>th</sup> European Conference on Antennas and Propagation (EuCAP 2012)*, vol. 1, pp. 2206–2208, Prague, Czech Republic, March 2012.
- [33] S. Mercader-Pellicer, W. Tang, D. Bresciani, H. Legay, N. J. G. Fonseca, and G. Goussetis, "Angularly stable linear-to-circular polarizing reflectors for multiple beam antennas," in *IEEE Trans. Antennas Propag.*, DOI 10.1109/TAP.2020.3048494
- [34] S. M. A. M. H. Abadi, and N. Behdah, "Wideband linear-to-circular polarization converters based on miniaturized-element frequency selective surfaces," in *IEEE Trans. Antennas Propag.*, vol. 64, no. 2, pp. 525–534, Feb. 2016.
- [35] D. Blanco, and R. Sauleau, "Broadband and broad-angle multilayer polarizer on hybrid optimization algorithm for low-cost Ka-band application," in *IEEE Trans. Antennas Propag.*, vol. 66, no. 4, pp. 1874–1881, April 2018.
- [36] D. M. Pozar, "Microwave engineering," 3rd Ed. Hoboken, NJ, USA.: Wiley, 2005.
- [37] O. A. Peverini et al., "Selective Laser Melting Manufacturing of Microwave Waveguide Devices," in *Proceedings of the IEEE*, vol. 105, no. 4, pp. 620–631, April 2017.
- [38] R. G. Edwards, C. M. Norton, J. E. Campbell and D. Schurig, "Effective Conductivity of Additive-Manufactured Metals for Microwave Feed Components," in *IEEE Access*, vol. 9, pp. 59979–59986, 2021
- [39] A. Charles, A. Elkaseer, L. Thijs, V. Hagenmeyer, S. Scholz, "Effect of Process Parameters on the Generated Surface Roughness of Down-Facing Surfaces in Selective Laser Melting," in *Appl. Sci.* 2019, 9, 1256.
- [40] P. Booth and E. V. Lluich, "Enhancing the Performance of Waveguide Filters Using Additive Manufacturing," in *Proceedings of the IEEE*, vol. 105, no. 4, pp. 613–619, April 2017.
- [41] A. Dorlé et al., "Circularly Polarized Leaky-Wave Antenna Based on a Dual-Mode Hollow Waveguide," in *IEEE Transactions on Antennas and Propagation*, vol. 69, no. 9, pp. 6010–6015, Sept. 2021
- [42] S. Sirci, E. Menargues and M. Billod, "Space-qualified Additive Manufacturing and its Application to Active Antenna Harmonic Filters", 2021 IEEE MTT-S International Microwave Filter Workshop (IMFW), Perugia, Italy, Nov. 2021
- [43] Thomas Keating Ltd. [online]. Available: <https://www.terahertz.co.uk>
- [44] C. Pfeiffer and B. Tomasic, "Multi-octave linear-to-circular polarizers," 2017 IEEE International Symposium on Antennas and Propagation UNSC/URSI National Radio Science Meeting, 2017



**Carlos Molero** was born in Seville, Spain, in April 1987. He received the Licenciado and Ph.D. degrees from the Universidad de Sevilla, Seville, Spain in 2011 and 2017 respectively, both in Physics. From March 2017 to July 2020 he has been a postdoc in INSA Rennes, Rennes, France. He is currently working at Universidad de Granada, Granada, Spain, as a postdoc. His research interests focus on the study of periodic structures, both in planar and 3D architectures, circuit models, full-metal devices, new conception of polarizers based on 3D printable self-supported cells and metasurfaces in general. Dr. Molero was a recipient of some prizes, as the Best Engineer Prize in the European Microwave Conference of 2015 in Paris.



**Hervé Legay** received the electrical engineering and Ph.D. degrees from the National Institute of Applied Sciences, Rennes, France, in 1988 and 1991, respectively. He was then a Post-Doctoral Fellow with the University of Manitoba, Winnipeg, MB, Canada. In 1994, he joined Alcatel Space (now Thales Alenia Space), Toulouse, France. He initially conducted studies in the areas of military telecommunication satellite antennas and antenna processing. He designed the architecture and the antijamming process of the Syracuse 3 active antenna. He is currently

the Head of the R&T on space antennas, developing new antenna concepts with emerging technologies (Reflectarrays, integrated antennas, multiple beam quasi-optical antennas, innovative active architectures, antenna processing,...). He is co-Director of the joint laboratory MERLIN, involving Thales Alenia Space, and the Institut d'Electronique et de Télécommunication de Rennes. Dr. Legay is the Chair of a group of Antenna Experts in Thales Group. He coordinates the collaborations with academic and research partners. He has authored 40 patents. He was a co-prize winner of the 2007 Schelkunoff Prize Paper Award. He was a recipient of the Gold Thales Awards in 2008, a reward for the best innovations in the Thales Group.



**Thierry Pierré** , photograph and biography not available at the time of publication.



**María García Viguera** was born in Murcia, Spain. She received the M.Sc. degree in telecommunications engineering and the Ph.D. degree from the Technical University of Cartagena, Cartagena, Spain, in 2007 and 2012, respectively. From 2012 to 2015, she was a Research Fellow with the Laboratory of Electromagnetism and Antennas, École Polytechnique Fédérale de Lausanne, Lausanne, Switzerland. She is currently an Assistant Professor with the Institute National des Sciences Appliquées de Rennes, Rennes, France. She has coauthored more than 20

IEEE journals and 40 publications in international conferences. Her current research interests include leaky wave antennas, periodic surfaces, waveguide feed chain components, and the evaluation of additive manufacturing's potential for RF design.

Dr. García-Viguera was a recipient of several prizes, including two Best Ph.D. Thesis awards from COI/AEIT in 2014 and UPTC in 2013, respectively, in Spain, and Best Paper Awards in MAPE 2013 in Chengdu, and EuCAP 2012 in Prague.